Real-time observation of intramolecular proton transfer in the electronic ground state of chloromalonaldehyde: An *ab initio* study of time-resolved photoelectron spectra

Márcio T. do N. Varella, Yasuki Arasaki, Hiroshi Ushiyama, and Kazuo Takatsuka
Department of Basic Science, Graduate School of Arts and Sciences, University of Tokyo, Komaba, Tokyo 153-8902, Japan

Kwanghsi Wang and Vincent McKoy
Laboratory for Molecular Sciences, California Institute of Technology, Pasadena, California 91125

(Received 11 September 2006; accepted 14 December 2006; published online 2 February 2007)

The authors report on studies of time-resolved photoelectron spectra of intramolecular proton transfer in the ground state of chloromalonaldehyde, employing *ab initio* photoionization matrix elements and effective potential surfaces of reduced dimensionality, wherein the couplings of proton motion to the other molecular vibrational modes are embedded by averaging over classical trajectories. In the simulations, population is transferred from the vibrational ground state to vibrationally hot wave packets by pumping to an excited electronic state and dumping with a time-delayed pulse. These pump-dump-probe simulations demonstrate that the time-resolved photoelectron spectra track proton transfer in the electronic ground state well and, furthermore, that the geometry dependence of the matrix elements enhances the tracking compared with signals obtained with the Condon approximation. Photoelectron kinetic energy distributions arising from wave packets localized in different basins are also distinguishable and could be understood, as expected, on the basis of the strength of the optical couplings in different regions of the ground state potential surface and the Franck-Condon overlaps of the ground state wave packets with the vibrational eigenstates of the ion potential surface. © *2007 American Institute of Physics*. [DOI: 10.1063/1.2432119]

I. INTRODUCTION

Proton transfer is a fundamental process in chemistry and biology and have long been identified as a key mechanism underlying the properties of many important systems ranging from water to proteins and DNA.[1–4] Though much effort has been focused on tunneling splitting in the ground state,[5–16] dynamical aspects such as long-range coupling to internal rotation[17,18] and the mechanism of double proton transfer[19] have been addressed. Proton transfer dynamics in electronically excited states have also been explored in real-time studies[20–24] and Lochbrunner *et al.* have demonstrated the utility of pump-probe photoelectron spectroscopy for probing the dynamics of intramolecular proton transfer in excited states.[25] Exploring the direct dynamics of proton transfer in the electronic ground state via time-resolved photoelectron spectroscopy would seem timely and of interest.

The use of time-resolved photoelectron spectroscopy as a probe of wave packet dynamics is becoming widespread.[25–31] In contrast to other probes, there are no dark states and the method is well suited for following the dynamics along all energetically allowed internuclear distances simultaneously in a pump-probe experiment. We recently carried out model studies of real-time observation of proton transfer by means of dump-probe photoelectron spectroscopy.[32,33] The extension from linear[34] to polyatomic molecules poses a number of difficulties, the most severe being the high dimensionality of the problem. Proton motion is usually coupled to many other vibrational modes of the system (molecular backbone) and the computational effort associated with full-dimensional quantum mechanical descriptions can become prohibitive. This limitation is even more severe in studies of time-resolved photoelectron spectra where ionization leads to a continuum of photoelectron energies, i.e., infinitely many potential energy surfaces are coupled in the photoionization process, and the requisite numerical quadrature gives rise to a twofold multidimensionality because there are proton and skeletal modes on each potential surface of the discretized continuum.

To address these difficulties, we recently proposed a simple but broadly applicable method for generating effective potential energy surfaces of reduced dimensionality, wherein the coupling between reaction and substrate modes is embedded through spatial and temporal averaging over an ensemble of classical trajectories.[33] These time-independent classically averaged potential surfaces significantly reduce the computational effort in studies of time-resolved photoelectron spectra of multidimensional reactions and account for proton-substrate coupling in an average sense, thus providing a more realistic description than the usual sudden (frozen geometry) or adiabatic (local optimal geometry) approximations for the molecular skeleton. For studies of time-resolved photoelectron spectra, the classically averaged potential surfaces are more suitable than system-bath schemes such as the Cartesian reaction surface.[35–37] These schemes assume time-dependent effective potentials for the proton,

 © 2007 American Institute of Physics

Downloaded 06 Feb 2007 to 131.215.225.9. Redistribution subject to AIP license or copyright, see http://jcp.aip.org/jcp/copyright.jsp

which poses some difficulties in the description of the optical couplings,[33] and the harmonic approximation for the substrate modes, which becomes inadequate for vibrational energies around and above the transition state.

A further technical difficulty in studies of time-resolved photoelectron spectra of multidimensional systems is the computational cost of the photoionization matrix elements. Though the dynamical content of time-resolved photoelectron spectra is determined by the dependence of the underlying matrix elements on molecular geometry, accurate estimates of these matrix elements are time consuming and, to our knowledge, the only *ab initio* calculation of time-resolved photoelectron cross sections reported for a polyatomic system[38] included just two vibrational modes. Because the complete neglect of other vibrational coordinates can be overly restrictive, the classically averaged potentials provide a convenient framework for embodying multidimensional effects (in an average sense) in the matrix elements without a concomitant increase in computational effort. In the present application, *ab initio* estimates were obtained over a two-dimensional reaction grid for the proton, $\mathbf{R}=(x,y)$, but for a skeleton geometry that changes as a function of $\mathbf{R}$, in accordance with the classical averages.

In previous studies proton motion was described with a two-dimensional wave packet in the molecular plane and vibrational energy redistribution and relaxation due to coupling with skeletal degrees of freedom were either neglected[32] or incorporated through classically averaged potential surfaces.[33] The initial condition was assumed to be a wave packet (either a vibrational eigenstate or a coherent superposition) on the potential surface of an excited state, which was optically dumped to the ground state and subsequently ionized by a time-delayed probe pulse, assuming geometry-independent photoionization matrix elements (Condon approximation). In this paper we seek to extend our model in two ways, namely, by generating vibrationally hot wave packets in the ground state surface from a realistic initial condition and by probing the photoelectron spectra with geometry-dependent matrix elements. We consider the pump-dump-probe scheme of Fig. 1, where a linearly polarized pulse of frequency ω_{pu} pumps a wave packet from the ground electronic state to an excited state, where it is dumped by a time-delayed (ΔT_{du}) pulse of frequency ω_{du}, giving rise to vibrationally hot population in the ground state that is subsequently probed by a third time-delayed (ΔT_{pr}) pulse of frequency ω_{pr}. The molecule is assumed to be initially in its vibrational ground sate, since gases with low vibrational temperatures are routinely produced by supersonic jet cooling.[39]

After the present study was completed, we became aware of the recent work by Coe and Martínez,[40] showing that the S_2 excited state of malonaldehyde undergoes rapid *cis-trans* isomerization (rotation around the C=C bond in the chelate ring). As we will discuss in more detail below, similar out-of-plane motion also appears to occur in excited chloromalonaldehyde (Cl-MA). Because this process competes with proton transfer and was not included in our nuclear dynamics, our results will not be quantitative; however, they do demonstrate that photoelectron signals can be used to monitor proton transfer. In this sense Cl-MA constrained to planar geometry may serve as a useful model for systems in which out-of-plane rotation is hindered.

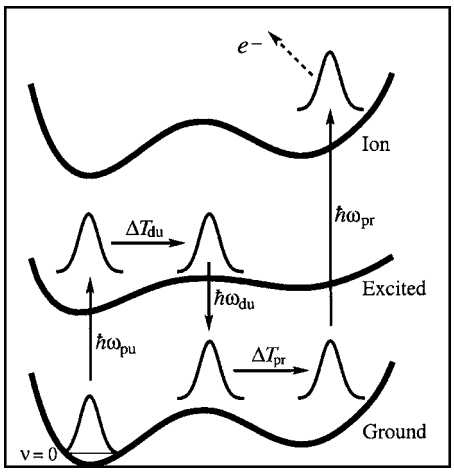

FIG. 1. The pump-dump-probe scheme for chloromalonaldehyde. A linearly polarized pulse of frequency ω_{pu} pumps a wave packet from the ground electronic state to an excited state, where it is dumped by a time-delayed (ΔT_{du}) pulse of frequency ω_{du} and subsequently probed by a third time-delayed (ΔT_{pr}) pulse of frequency ω_{pr}.

The outline of this paper is as follows. In the next section we describe our formulation of pump-dump-probe time-resolved photoelectron spectroscopy focusing on the use of classically averaged potential surfaces and the scaling of the numerical effort arising with multidimensional wave packets and use of *ab initio* photoionization matrix elements. In Sec. III we discuss the preparation of vibrationally hot wave packets by pumping from the vibrational ground state and dumping with a time-delayed pulse, while the probing of intramolecular proton transfer with time- and energy-resolved photoelectron signals is discussed in Sec. IV. Our concluding remarks are given in Sec. V.

II. THEORY OUTLINE

The formulation of pump-probe time-resolved photoelectron spectroscopy has been discussed elsewhere,[34] as well as its modifications to account for target rotation[41] and nonadiabatic couplings.[42] Generalization to the present pump-dump-probe scheme is straightforward and only a few aspects related to the scaling of the computational effort in applications to multidimensional systems and the use of classically averaged effective potential surfaces will be discussed here.

A. Time-resolved pump-dump-probe photoelectron spectroscopy

In the pump-dump-probe scheme of Fig. 1, vibrationally hot population is generated in the electronic ground state by pumping the lowest vibrational eigenstate to an electronically excited state with a linearly polarized pulse of frequency ω_{pu} and dumping with a time-delayed (ΔT_{du}) pulse of frequency ω_{du}. The nonstationary wave packet is subse-

Downloaded 06 Feb 2007 to 131.215.225.9. Redistribution subject to AIP license or copyright, see http://jcp.aip.org/jcp/copyright.jsp

quently probed with a third time-delayed (ΔT_{pr}) pulse of frequency ω_{pr}, and the time evolution of the system is governed by the following set of coupled equations:[34]

$$i\hbar\frac{\partial}{\partial t}\chi_g(\mathbf{X},t) = [T_N + V_g(\mathbf{X})]\chi_g(\mathbf{X},t) + V_{pd}(t)\mu_{ge}(\mathbf{X})\chi_e(\mathbf{X},t) + V_{pr}(t)\sum_{j=1}^{N_k}\sum_{lm} C^*_{lm}(\mathbf{X},k_j,\Omega_X,\theta_P)\chi_{k_jlm}(\mathbf{X},t), \tag{1}$$

$$i\hbar\frac{\partial}{\partial t}\chi_e(\mathbf{X},t) = [T_N + V_e(\mathbf{X})]\chi_e(\mathbf{X},t) + V_{pd}(t)\mu_{eg}(\mathbf{X})\chi_g(\mathbf{X},t), \tag{2}$$

and

$$i\hbar\frac{\partial}{\partial t}\chi_{k_jlm}(\mathbf{X},t) = \left[T_N + V_{ion}(\mathbf{X}) + \frac{(\hbar k_j)^2}{2m_e}\right]\chi_{k_jlm}(\mathbf{X},t) + V_{pr}(t)C_{lm}(\mathbf{X},k_j,\Omega_X,\theta_P)\chi_g(\mathbf{X},t), \tag{3}$$

where χ_g, χ_e, and χ_{k_jlm} are wave packets on the ground (V_g), excited (V_e), and ion (V_{ion}) potential energy surfaces (PES's), respectively. T_N is the kinetic energy operator for the nuclei, $\mathbf{X}$ denotes the nuclear coordinates in a space-fixed frame (defined by the polarization directions of the laser fields), m_e is the electron mass, and k_j are radial quadrature points (N_k is the number of such points) for the numerical integration over photoelectron linear momenta (angular integrations are carried out analytically by expanding the continuum wave function in spherical harmonics). The time-dependent amplitudes V_{pd} and V_{pr} are related to the pump-dump and probe stages, respectively, and may be explicitly written as

$$V_{pd}(t) = -E_{pu}f_{pu}(t)\sin(\omega_{pu}t) - E_{du}f_{du}(t-\Delta T_{du})\sin(\omega_{du}t), \tag{4}$$

$$V_{pr}(t) = -E_{pr}f_{pr}(t-\Delta T_{du}-\Delta T_{pr})\sin(\omega_{pr}t), \tag{5}$$

where $E_{du,pu,pr}$ and $f_{du,pu,pr}$ are electric field strengths and Gaussian envelopes, respectively. Finally, $\mu_{ge}=\mu_{eg}$ is the electronic dipole transition amplitude, and the C_{lm} coefficients in Eqs. (1) and (3) provide the underlying dynamical information on the photoionization process,[34]

$$C_{lm}(\mathbf{X},k_j,\Omega_X,\theta_P) = \sqrt{\frac{4\pi}{3}}\sum_{\lambda\mu} I_{l\lambda\mu}(\mathbf{X},k_j)D^{l*}_{\lambda m}(\Omega)D^1_{\mu 0}(\Omega), \tag{6}$$

where the $I_{l\lambda\mu}$ are partial wave photoionization matrix elements in the molecular frame, $D^l_{\lambda m}$ are Wigner rotation matrices,[43] and Ω collectively denotes the Euler angles defining the transformation from the molecule-fixed frame to the space-fixed frame. In Eq. (6), the polarization vector of the probe pulse is assumed to lie in the $\hat{z}$ direction of the space-fixed frame. The molecule is oriented at angles $\Omega_X=(\phi_X,\theta_X,\gamma_X)$ with respect to the polarization vector of the dump field, and θ_P is the angle between the dump and probe vectors (though the more general case would pose no difficulty, the pump and dump fields are assumed parallel for simplicity). The iterative procedure employed to obtain the *ab initio* photoionization matrix elements ($I_{l\lambda\mu}$) is based on the Schwinger variational principle and has been fully discussed elsewhere.[44]

In a compact matrix notation, Eqs. (1)–(3) may be written as

$$i\hbar\frac{\partial}{\partial t}\Psi(\mathbf{X},t) = \hat{\mathbf{H}}(\mathbf{X},t)\Psi(\mathbf{X},t) = [\hat{\mathbf{T}}(\mathbf{X}) + \hat{\mathbf{V}}_D(\mathbf{X}) + \hat{\mathbf{V}}_O(\mathbf{X})]\Psi(\mathbf{X},t), \tag{7}$$

$$\Psi(\mathbf{X},t) = \begin{pmatrix} \chi_g(\mathbf{X},t) \\ \chi_e(\mathbf{X},t) \\ \vdots \\ \chi_{k_jlm}(\mathbf{X},t) \\ \vdots \end{pmatrix}, \tag{8}$$

with a similar convention for the matrix operators. $\hat{\mathbf{T}}$ is a diagonal matrix representing the kinetic energy operator and can be treated by fast Fourier transform techniques, as usual.[45] $\hat{\mathbf{V}}_D$ is also a diagonal matrix composed of PES's for the ground, excited, and ion states. The coupling induced by the laser fields is contained in the off-diagonal matrix $\hat{\mathbf{V}}_O$, which couples the ground state to the excited bound state as well as to the ion states. These time-dependent equations are solved using the split-operator technique[45,46] and the resulting working expressions for the time evolution of nuclear wave packets are given elsewhere.[34] Numerical solution of these coupled Schrödinger equations for polyatomic molecules is computationally challenging since Eq. (7) is multidimensional in two ways: the state vectors have ($N_{ion}+2$) components, where N_{ion} is the number of final ion channels (k_j,l,m), and each such component is a multidimensional vibrational wave packet. The angular resolution of photoelectrons for large systems with low symmetry requires many (k_j,l,m) surfaces (hundreds to thousands), which combined with a large number of vibrational modes (wave packet dimension) may well make the computational effort prohibitive.

B. Classically averaged potential energy surfaces

The unusually large number of optically coupled potential surfaces involved in studies of time-resolved photoelectron spectra and the different skeletal modes often participating in proton transfer reactions require a strategy that reduces the dimensionality of the dynamical system, but does not completely neglect vibrational energy redistribution and coupling between proton motion and backbone vibrations. Because the high vibrational energies of interest in these spectroscopic studies hinder the use of proton-substrate schemes wherein the proton wave packet is coupled to a bath of harmonic oscillators, we recently proposed a method for obtaining time-independent potential surfaces of reduced dimensionality that embed proton-skeleton couplings by averaging over an ensemble of classical trajectories.[33] Distinguishing

Downloaded 06 Feb 2007 to 131.215.225.9. Redistribution subject to AIP license or copyright, see http://jcp.aip.org/jcp/copyright.jsp

between reaction ($\mathbf{R}$) and substrate ($\mathbf{Q}$) coordinates, $\mathbf{X}=(\mathbf{R},\mathbf{Q})$, the semiclassical Wigner distribution function associated with the nuclear wave packet $\varphi(\mathbf{R},\mathbf{Q},t)$ may be written as

$$\Gamma_{\varphi}(\mathbf{R}_i(t),\mathbf{P}_i(t),\mathbf{Q}_i(t),\mathbf{\Pi}_i(t)), \tag{9}$$

and propagated in terms of classical trajectories $(\mathbf{R}_i(t),\mathbf{P}_i(t),\mathbf{Q}_i(t),\mathbf{\Pi}_i(t))$ with the subscript i labeling the trajectories, and $\mathbf{P}$ and $\mathbf{\Pi}$ the linear momenta associated with $\mathbf{R}$ and $\mathbf{Q}$, respectively. If we now divide the reaction configuration space into several small regions $\mathbf{R}^{(a)}$, $a=1,2,\ldots$, and average over substrate coordinates $\mathbf{Q}$ whenever trajectories cross each such region, it is reasonable to regard the reaction-coordinate wave packet as propagating on the effective time-dependent potential

$$V(\mathbf{R}^{(a)},\langle\mathbf{Q}(\mathbf{R}^{(a)},t)\rangle_{\varphi}), \tag{10}$$

where the skeleton positions, averaged over the set of trajectories, are placed at

$$\langle\mathbf{Q}(\mathbf{R}^{(a)},t)\rangle_{\varphi}=\sum_i \Gamma_{\varphi}(\mathbf{R}_i^{(a)}(t),\mathbf{P}_i(t),\mathbf{Q}_i(t),\mathbf{\Pi}_i(t))\mathbf{Q}_i(t), \tag{11}$$

whenever the reaction coordinates are found in region $\mathbf{R}^{(a)}$. For application to studies of time-resolved photoelectron spectra, it is advantageous to further remove the time dependence from the potential of Eq. (10) by averaging over time and initial conditions,

$$\langle\langle\mathbf{Q}(\mathbf{R}^{(a)})\rangle\rangle=\frac{1}{T}\int_0^T dt\int d\varphi\langle\mathbf{Q}(\mathbf{R}^{(a)},t)\rangle_{\varphi}, \tag{12}$$

thus resulting in an effective potential for the reaction coordinates that depends neither on time nor on the choice of the initial reduced wave packet, a convenient feature since the wave packets generated by pumping and dumping have arbitrary shapes.

In practice, an ensemble of M trajectories may be generated for a system with $(N+2)$ atomic coordinates, namely, two reaction coordinates, $\mathbf{R}=(x,y)$, and N substrate coordinates; the reaction-coordinate configuration space may then be arbitrarily divided into regions $x_1<x_2<x_3<\cdots$ and $y_1<y_2<y_3<\cdots$, thus defining small segments $s_{ij}=(x_i,y_j\leqslant y<y_{j+1})$, where it is assumed that proton transfer takes place along the Ox direction. For every s_{ij} we may examine the entire set of trajectories and record all the times when the reaction coordinates cross each segment. If the reaction coordinates cross the s_{ij} segment n_{ij}^{α} times in the αth trajectory, the total number of crossings in this particular segment (N_{ij}) is obtained by summing over the trajectories,

$$N_{ij}=\sum_{\alpha=1}^{M} n_{ij}^{\alpha}. \tag{13}$$

We now denote by $q_r^{\alpha\nu}(s_{ij})$ the value of the rth skeleton coordinate when the reaction coordinates cross s_{ij} for the νth time in the αth trajectory. An average value for each substrate coordinate may be obtained as

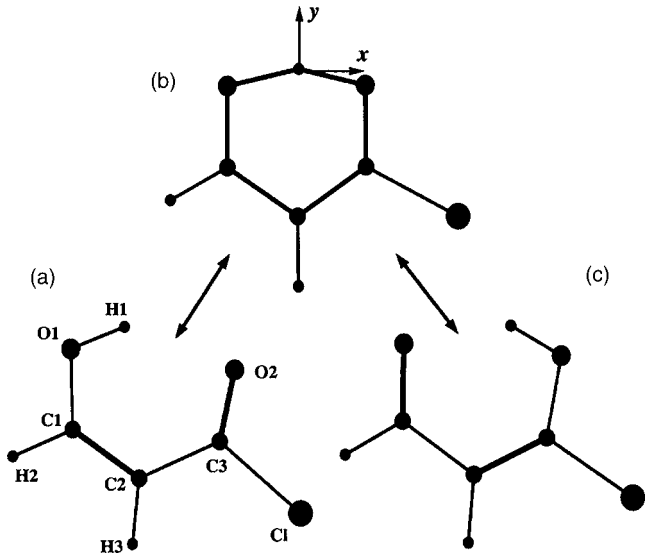

FIG. 2. Intramolecular proton transfer in the ground state of chloromalonaldehyde. Structure (a) is the most stable (global minimum), (b) is the transition state, and (c) is the secondary minimum. The frame of reference for the reaction coordinates is shown in structure (b).

$$\bar{q}_r(s_{ij})=\frac{1}{N_{ij}}\sum_{\alpha=1}^{M}\sum_{\nu=1}^{n_{ij}^{\alpha}} q_r^{\alpha\nu}(s_{ij}). \tag{14}$$

Hence, the vector $(\bar{q}_1(s_{ij}),\bar{q}_2(s_{ij}),\ldots,\bar{q}_N(s_{ij}))$ could be viewed as representing the dynamically averaged skeleton geometry when the proton is found in the s_{ij} segment [note that Eq. (14) is an approximation to Eq. (12)]. The dynamics of the Cartesian reaction coordinates may hence be described with the time-independent effective Hamiltonian of reduced dimensionality given by

$$H(\mathbf{R},\mathbf{P})=T_{\mathbf{R}}+V_{\bar{\mathbf{Q}}}(\mathbf{R}), \tag{15}$$

where $\bar{\mathbf{Q}}(\mathbf{R})\equiv\{\bar{q}_1(\mathbf{R}),\ldots,\bar{q}_N(\mathbf{R})\}$ arises from the classical bath averaging of Eq. (12) and incorporates skeleton relaxation in an average sense, thus providing a reasonable approximation for studies of time-resolved photoelectron spectra. Kinetic energy couplings between $\mathbf{R}$ and $\mathbf{Q}$ coordinates are omitted in Eq. (15), and though these couplings[47,48] would be necessary to obtain quantitative results and realistic descriptions of proton transfer periods or dwell time between successive transfers, we choose the simplicity of Eq. (15) since it is expected to correctly describe the qualitative changes in photoelectron signals arising from proton motion across the barrier.

C. Model system

The in-plane coordinates of the proton are taken as the reaction system, $\mathbf{R}=(x,y)$, and all the remaining coordinates are considered as belonging to the substrate. The stable planar structures of Cl-MA are schematically shown in Fig. 2, and the reaction-coordinate frame of reference is shown in structure (b), with the origin taken at the position of the proton in the optimal transition state geometry, and the Ox and Oy axes pointing rightward and upward, respectively. The effective potential surfaces for the ground, excited, and

Downloaded 06 Feb 2007 to 131.215.225.9. Redistribution subject to AIP license or copyright, see http://jcp.aip.org/jcp/copyright.jsp

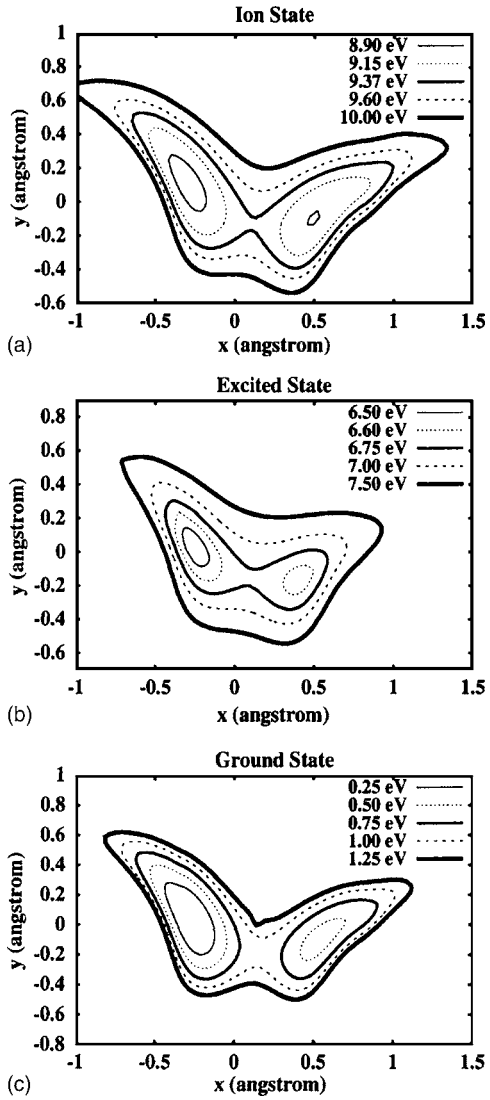

FIG. 3. Potential energy surfaces for the ground state (lower panel), excited state (central panel), and ion state (upper panel) of chloromalonaldehyde. All potential surfaces were calculated at the classically averaged geometry of the ground state.

ion states of Cl-MA are shown in Fig. 3. (How these surfaces are generated is discussed elsewhere.[33]) As the intermediate excited state for pumping and dumping, we employed the $2\,^1A'$ state, lying slightly above the first excited singlet state ($1\,^1A''$) except near the barrier between the two potential basins, because the former has a considerably larger transition dipole moment with the ground electronic state. The asymmetric potential arising from halogenation (Cl atom) conveniently enables distinction of wave packets on different sides of the transition state in studies of time-resolved photoelectron spectra. The lowest-energy geometry of the ground state [structure (a) in Fig. 2] corresponds to the left basin in the lower panel of Fig. 3.

Rotational motion is disregarded since Cl-MA has rotational constants around 1.4–8.7 GHz, implying rotation periods of $\sim 10^{-9}$ s. Since angular distributions of photoelectrons are not addressed here, we assume the polarization vectors of all laser pulses to be aligned with the molecular Oz axis (perpendicular to the molecular plane), because this orientation minimizes the number of ion surfaces (k_j,l,m).

D. Computational details

The procedure for sampling initial conditions and averaging over the set of classical trajectories to generate the effective potential surfaces is discussed elsewhere.[33] In short, classical molecular dynamics simulations were carried out employing quantum-chemical potential gradients obtained at the restricted Hartree-Fock level with the 6-31G(d,p) basis internal to the GAMESS package[49] and a locally analytic integrator.[50] The dipole transition amplitudes and PES's were obtained at the classically averaged geometry of the ground state because we assume vertical optical excitations and are probing proton transfer dynamics in the ground state. The PES's for the ground and ion states were determined at the HF level, while the PES for the excited state ($2\,^1A'$) was obtained from a single-excitation configuration-interaction calculation.

The wave packets and operators were represented on two-dimensional grids with lengths of 3.8 and 2.4 Å along the Ox and Oy directions, respectively, the number of points being $N_x=64$ and $N_y=32$. Integration over photoelectron momenta was carried out with a 50-point Simpson quadrature for $0 \leqslant k \leqslant 0.542$ a.u. (up to 4 eV), and the angular momentum of the photoelectron orbitals was expanded up to $l=6$, resulting in $N_{\text{ion}}=800$ symmetry-allowed (k_j,l,m) ion surfaces. The dimension of the state vector in Eq. (7) was therefore $N \simeq N_x \times N_y \times N_{\text{ion}} \simeq 1.64 \times 10^6$, indicating that studies of time-resolved photoelectron spectra would not be possible without employing potentials of reduced dimensionality (Cl-MA has a total of 21 vibrational degrees of freedom).

III. GENERATION OF VIBRATIONALLY HOT POPULATION IN THE GROUND STATE: PUMP-DUMP STAGE

Optical pumping has been widely employed to achieve efficient population transfer between quantum states and several strategies have been proposed for laser control of chemical reactions. The Brumer-Shapiro scheme[51] employs a sequence of lasers with well-defined frequencies (continuous wave limit) and varying phase relations, the Tannor-Rice-Kosloff scheme[52] takes advantage of the time delay between successive laser pulses, and the stimulated Raman adiabatic passage technique[53] uses a counterintuitive sequence of laser pulses to suppress the intermediate state population. In addition, the time-frequency coherence of light is exploited in optimal control techniques employing shaped pulses, which have been extensively studied theoretically[54–56] and experimentally.[57,58] In the present study we seek to generate vibrationally hot population in the ground state, and though infrared pumping has been applied to pump-probe dynamics,[59] we employ the more conventional strategy[60–64] of pumping to an excited state and dumping with a time-delayed pulse of different frequency.

The vibrational spectra of the ground ($1\,^1A'$) and excited ($2\,^1A'$) states were obtained with the energy screening method.[65] We adopt the notations S_0 and S_1 to label the electronic ground and excited states, respectively, as well as ν_0 and ν_1 for the corresponding vibrational eigenstates. The vibrational spectra are shown in Table I for selected eigenstates

Downloaded 06 Feb 2007 to 131.215.225.9. Redistribution subject to AIP license or copyright, see http://jcp.aip.org/jcp/copyright.jsp

TABLE I. Vibrational spectra for the ground (E_{ν_0}) and excited (E_{ν_1}) electronic states (eV) and their Franck-Condon factors. The vibrational levels of the ground (ν_0) and excited (ν_1) states are shown along columns and rows, respectively.

ν_0	E_{ν_0} \ ν_1 / E_{ν_1}	3 6.933	4 6.992	5 7.016	6 7.057	7 7.107
0	0.303	0.0011	0.0059	0.0054	0.0119	0.0002
8	0.949	0.0264	0.0094	0.0070	0.0003	0.0353
9	0.959	0.0850	0.2008	0.0003	0.0210	0.0124
10	1.022	0.1052	0.0509	0.0002	0.1296	0.0243
11	1.046	0.0000	0.0162	0.0636	0.1316	0.0464
12	1.088	0.0853	0.0028	0.0468	0.0252	0.0116
13	1.101	0.0093	0.0459	0.0189	0.0000	0.0570
14	1.109	0.0131	0.0792	0.0018	0.0060	0.0166
15	1.161	0.0718	0.0032	0.0008	0.0936	0.0070
16	1.195	0.0005	0.0009	0.0197	0.0131	0.0958
17	1.239	0.0226	0.0027	0.0003	0.0005	0.0494
18	1.248	0.0000	0.0185	0.0044	0.0058	0.0218
19	1.262	0.0003	0.0183	0.0008	0.0060	0.0100
20	1.312	0.0131	0.0171	0.0010	0.0002	0.0245
21	1.342	0.0069	0.0019	0.0180	0.0298	0.0355
22	1.356	0.0034	0.0310	0.0116	0.0606	0.0049

along with the corresponding Franck-Condon factors, $|\langle \nu_0 | \nu_1 \rangle|^2$. The $\nu_1=3-7$ levels clearly overlap appreciably (>0.01) with several eigenstates lying above the transition state in S_0 ($E_{TS}=0.936$ eV) and we thus tested several pump-dump schemes with $\hbar\omega_{pu}$ ranging from 6.63 eV (resonance with $\nu_1=3$) to 6.80 eV (resonance with $\nu_1=7$), and many different dump frequencies, time delays, and pulse widths. Though the final vibrationally hot population ($\nu_0>0$) often remained localized (in either basin) or evenly delocalized when the wave packets were mainly composed of $\nu_0 \leqslant 12$ eigenstates, it was possible to observe clear proton transfer employing lower dump frequencies (i.e., populating higher vibrational eigenstates in S_0). The final vibrationally hot population in the ground state (P_{hot}) may be defined through

$$1 = P_{S_0} + P_{S_1} \equiv (P_0 + P_{hot}) + P_{S_1}, \tag{16}$$

where P_0 is the population in the $\nu_0=0$ level. P_{hot} values ranging from 0.15 to 0.40 could be obtained for several (10^2) different pump-dump schemes (i.e., combinations of pulse parameters and time delays), often with laser intensities below 10^{12} W/cm^2. A few examples are shown in Table II (schemes i–v), and though the present two-dimensional model is not expected to account for a complete description of the actual multidimensional spectra, our results suggest that efficient population transfer to vibrationally hot levels might be achieved without very high laser intensities (i.e., multiphoton ionization would not be expected to be a serious drawback). The selected working cases are labeled A–D in Table II and the time evolution of the population in the ground ($P_{S_0}=P_0+P_{hot}$) and excited (P_{S_1}) states is shown in panel (a) of Fig. 4 for scheme B. The general trends are similar for all schemes, with high-frequency and low-amplitude oscillations when the two pulses are superimposed, and otherwise a smooth rise of P_{hot} (or lowering of P_0).

In all cases, there is significant final population in the $\nu_0=0$ level ($P_0 \simeq 0.4-0.6$), and we define the vibrationally hot left-population ratio (P_{left}^{hot}),

$$P_{left}^{hot} = \frac{P_{left} - P_0}{P_{S_0} - P_0} = \frac{P_{left} - P_0}{P_{hot}}, \tag{17}$$

where P_{left} is the population in the ground state potential located to the left of the transition state (the population of the $\nu_0=0$ level, P_0, remains localized in the left basin and does not transfer; see the ground state PES in Fig. 3). P_{left}^{hot} thus reflects proton transfer in the ground state and its time evolution for schemes A–D is shown in panel (b) of Fig. 4, where proton transfer is very clear in schemes A and B (thick and thin solid lines, respectively). The wave packet, however, alternates between delocalized and localized to the left in scheme C (long-dashed line) and remains delocalized in scheme D (short-dashed line). Our model gives rise to periodic motion in the ground state because real-time vibrational energy redistribution is not accounted for (couplings to the molecular backbone are incorporated in an average sense), but altogether schemes A–D may provide insight into the ability of time-resolved spectra to track proton motion, since they allow comparison between photoelectron signals arising from localized (in either basin) as well as delocalized wave

TABLE II. Parameters of different pump-dump schemes. Intensities (I) are given in 10^{11} W/cm^2, frequencies ($\hbar\omega$) in eV, widths (FWHM) in fs, and time delays (ΔT_{du}) in fs. The final vibrationally hot population in the ground state (P_{hot}) is also given.

	Pump field parameters			Dump field parameters				
Scheme	I_{pu}	$\hbar\omega_{pu}$	FWHM$_{pu}$	I_{du}	$\hbar\omega_{du}$	FWHM$_{du}$	ΔT_{du}	P_{hot}
i	6.32	6.69	60.0	8.60	5.87	40.0	60.0	0.152
ii	8.60	6.69	60.0	6.32	5.87	40.0	60.0	0.208
iii	17.5	6.71	60.0	2.81	5.87	50.0	50.0	0.377
iv	3.55	6.75	80.0	6.32	5.87	50.0	60.0	0.163
v	0.07	6.75	200.0	2.81	5.87	50.0	120.0	0.166
A	3.55	6.75	80.0	2.81	5.87	50.0	60.0	0.152
B	8.60	6.71	60.0	2.81	5.87	40.0	40.0	0.209
C	6.32	6.69	60.0	8.60	5.87	40.0	40.0	0.147
D	8.60	6.71	60.0	2.81	5.72	50.0	40.0	0.201

Downloaded 06 Feb 2007 to 131.215.225.9. Redistribution subject to AIP license or copyright, see http://jcp.aip.org/jcp/copyright.jsp

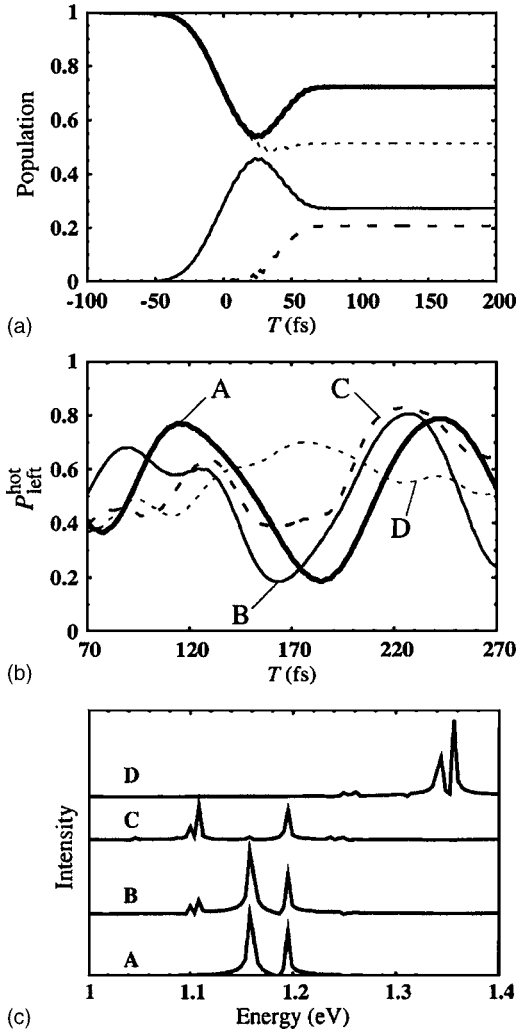

FIG. 4. Panel (a): time evolution of the population in the ground state (P_{S_0}, thick solid line) and excited state (P_{S_1}, thin solid line) for scheme B in Table II [the time origin is the center of the pump pulse in panels (a) and (b)]. The decomposition of P_{S_0} into the $\nu_0=0$ component (P_0, short-dashed line) and vibrationally hot components (P_{hot}, long-dashed line) is also shown. Panel (b): time evolution of $P_{\text{left}}^{\text{hot}}$ for schemes A (thick solid line), B (thin solid line), C (long-dashed line), and D (short-dashed line). Panel (c): decomposition of the final vibrationally hot population into the vibrational eigenstates of the ground (S_0) state for schemes A–D.

packets. Finally, we show in panel (c) of Fig. 4 the decomposition of the final ground state wave packet, $\chi_g(t_f)$, into the vibrational eigenstates of S_0,

$$S(E,t_f)=\int dt\,\exp\left(i\frac{Et}{\hbar}\right)\langle\chi_g(t_f)|\chi_g(t+t_f)\rangle, \tag{18}$$

where the $\nu_0=0$ peak is omitted in all cases. The very regular pattern observed for scheme A [panel (b), thick solid line] seems to arise from the superposition of essentially two levels, namely, $\nu_0=15$, and 16 ($E_{\nu_0}=1.161$ and 1.195 eV, respectively), corresponding to the two peaks of curve A [panel (c)], while some contribution from $\nu_0=13$ and 14 ($E_{\nu_0}=1.101$ and 1.109 eV, respectively) is observed in scheme B. These should account for the small-amplitude vibration around 100 fs [panel (c), thin solid line]. The wave packet arising from scheme C is composed mainly of $\nu_0=13$, 14, and 16 eigenstates, and the lower dump frequency ($\hbar\omega_{\text{du}}$)

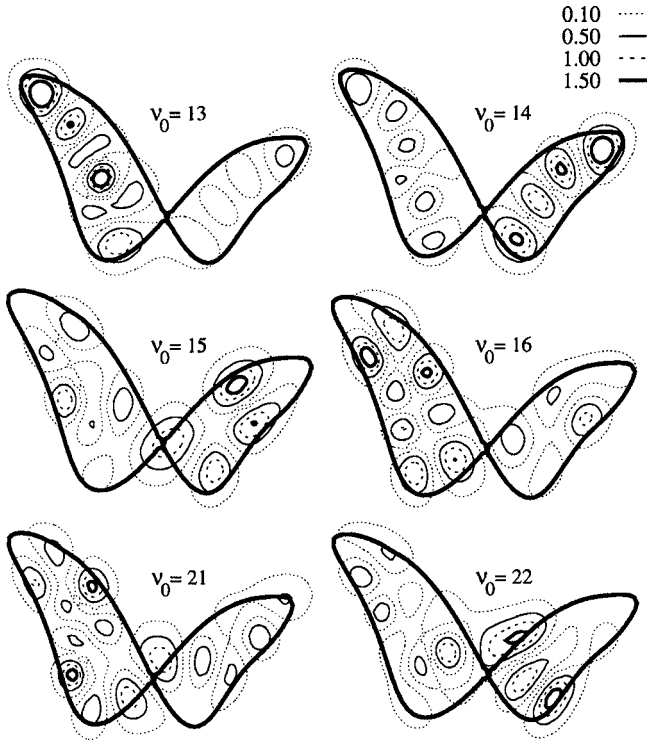

FIG. 5. Contour plots of selected vibrational eigenstates of the electronic ground state. In all panels, the contour of the ground state potential surface at the transition state energy ($E_{\text{TS}}=0.936$ eV) is also shown (thickest solid lines).

employed in scheme D (see Table II) strongly couples $\nu_0=21$ and 22 ($E_{\nu_0}=1.342$ and 1.356 eV, respectively). To provide insight into the wave packets' components, contour plots of the dynamically relevant vibrational eigenstates of the S_0 surface ($\nu_0=13$, 14, 15, 16, 21, and 22) are shown in Fig. 5.

IV. TIME-RESOLVED PHOTOELECTRON SPECTRA

As discussed elsewhere,[34] energy-resolved photoelectron signals,

$$P(\epsilon_k,\Delta T)=\sum_{lm}\frac{m_e k}{\hbar^2}\int d\mathbf{R}|\chi_{klm}(\mathbf{R},\Delta T,t_f)|^2, \tag{19}$$

and integrated photoelectron signals,

$$P_{\text{ion}}(\Delta T)=\int d\epsilon_k P(\epsilon_k,\Delta T), \tag{20}$$

may be readily obtained from the wave packets in Eqs. (1)–(3), where $\epsilon_k=(\hbar k)^2/2m_e$, t_f is a long time after the probe is switched off, and $\Delta T=(\Delta T_{\text{pu}}+\Delta T_{\text{pr}})$ is the total time delay. Below we present pump-dump-probe simulations of time-resolved photoelectron spectra wherein vibrationally hot wave packets are generated with schemes A–D.

A. Photoionization matrix elements

In previous studies of wave packet dynamics employing classically averaged potential surfaces and constant photoionization matrix elements (Condon approximation),[33] proton transfer could be tracked because Franck-Condon over-

Downloaded 06 Feb 2007 to 131.215.225.9. Redistribution subject to AIP license or copyright, see http://jcp.aip.org/jcp/copyright.jsp

TABLE III. Partial wave components (l,λ) of the outermost a'' occupied orbital of chloromalonaldehyde, where l and λ are, respectively, the angular momentum and its projection on the quantization axis of the molecular frame (Oz, perpendicular to the molecular plane in Fig. 2). *Left basin* and *right basin* correspond to ($x=-0.34$ Å, $y=0.08$ Å) and ($x=0.65$ Å, $y=0.08$ Å), respectively.

(l,λ)	Left basin	Right basin
(1,0)	0.107	0.263
(2,1)	0.198	0.157
(3,0)	0.011	0.022
(3,2)	0.054	0.052
(4,1)	0.044	0.035
(4,3)	0.013	0.009

laps between the ground and ion states were more favorable to the right of the transition state, thus giving rise to more intense signals for ionization from the right basin.

Studies of the geometry dependence of the photoionization cross sections also show that they are shape resonance enhanced in the right basin (proton closer to the Cl atom), suggesting that inclusion of this dependence in studies of time-resolved spectra should permit a clearer distinction between photoelectron signals arising from wave packets localized on different sides of the barrier. A partial wave expansion of the outermost orbital (a'') about the center of mass of the molecule shows increasing p character ($l=1$) as the proton transfers from the left basin to the right basin. For example, the first six partial wave components of this orbital around the left basin at ($x=-0.34$ Å, $y=0.08$ Å) and the right basin at ($x=0.65$ Å, $y=0.08$ Å) are shown in Table III. The partial wave (l,λ) expansions actually employed in the calculation provide a normalization better than 0.999, where l and λ are, respectively, the angular momentum and its projection on the principal axis (Oz), with the Ox and Oy axes lying in the σ_h plane (the molecular plane in Fig. 2). As the proton transfers across the barrier, the ka'' contribution to the photoionization cross section is strongly enhanced with peak heights for each proton position shifting to higher kinetic energy, as shown in Table IV, thus indicating that the stronger p character of the outermost orbital in the right basin enhances the photoionization cross sections.

TABLE IV. Resonant peaks in the partial photoionization cross sections (ka'' component) along the Ox direction of the reaction configuration space (the proton moves from the left to the right as x increases). *Energy* and *height* indicate the positions and heights of the partial cross section peaks, respectively.

x (Å)	Energy (eV)	Height (Mb)
−1.15	0.30	1.97
−0.45	0.30	1.11
−0.15	0.30	1.41
0.05	0.30	3.11
0.25	0.30	12.13
0.45	0.30	26.83
0.65	0.40	36.74
0.85	0.55	38.84
1.35	0.65	44.10
1.85	0.80	46.90

TABLE V. Absolute values of partial wave components (l,λ) of the ka'' photoionization matrix elements, where l and λ are, respectively, the angular momentum and its projection on the quantization axis of the molecular frame (Oz, perpendicular to the molecular plane in Fig. 2). *Left basin*, *barrier,* and *right basin* correspond to ($x=-0.34$ Å, $y=0.08$ Å), ($x=-0.05$ Å, $y=0.08$ Å), and ($x=0.65$ Å, $y=0.08$ Å), respectively.

(l,λ)	Left basin	Barrier	Right basin
(1,0)	0.030	0.179	1.030
(2,1)	0.141	0.132	0.389
(3,0)	0.039	0.080	0.710
(3,2)	0.194	0.226	0.867
(4,1)	0.050	0.087	0.340
(4,3)	0.140	0.154	0.372
(5,0)	0.004	0.005	0.010
(5,2)	0.011	0.015	0.038
(5,4)	0.018	0.021	0.073

The partial wave components of the photoelectron matrix elements can provide some additional insight into these changes, as shown in Table V. Around the left basin at ($x=-0.34$ Å, $y=0.08$ Å) and for a kinetic energy of $\epsilon_k=0.3$ eV, the leading photoelectron matrix elements for the ka'' continuum (velocity form) are considerably smaller than those near the right basin at ($x=0.65$ Å, $y=0.08$ Å) for $\epsilon_k=0.4$ eV. Intermediate values are found near the barrier at ($x=-0.05$ Å, $y=0.08$ Å) for $\epsilon_k=0.30$ eV, and these matrix elements show the extensive underlying angular momentum coupling in the photoelectron wave function in the right basin. This behavior will be richly reflected in the photoelectron dynamics, particularly in the angular distributions. These angular distributions will be discussed in a separate paper.

To gain further insight into the geometry dependence of the dynamical couplings (C_{lm}), we define the intensity

$$I(\mathbf{R},\theta_P,\Omega)=\int k^2 dk \sum_{lm} |C_{lm}(\mathbf{R},\theta_P,\Omega,k)|^2, \tag{21}$$

which depends on the orientation of the molecule and polarization directions of the laser pulses. If the polarization vectors of the pump, dump, and probe fields, as well as the molecular Oz axis, are assumed parallel only the ka' component contributes to Eq. (21), and the intensity for this particular orientation is shown in panel (a) of Fig. 6. Despite the absence of shape resonances (and hence of sharp peaks in the corresponding photoionization cross sections) in the ka' continuum, intensities increase significantly from the left to the right basin. However, in this case, the ability to distinguish between ionization from the left and the right basins would be expected to be poorer than with the resonance enhanced behavior of the ka'' component. In fact, if the polarization vector of the probe pulse ($\hat{\epsilon}_{\mathrm{pr}}$) is rotated by $\theta_P=\pi/2$, thus becoming perpendicular to $\hat{\epsilon}_{\mathrm{pu}}$, $\hat{\epsilon}_{\mathrm{du}}$ and the molecular principal axis, only the ka'' component contributes to Eq. (21), thus strongly enhancing the relative strength between optical couplings on the right and left basins, as shown in panel (b) of Fig. 6. These parallel ($\theta_P=0$, ka' component) and perpendicular ($\theta_P=\pi/2$, ka'' component) orientations may provide lower and upper bounds, respectively, for the resolution of

Downloaded 06 Feb 2007 to 131.215.225.9. Redistribution subject to AIP license or copyright, see http://jcp.aip.org/jcp/copyright.jsp

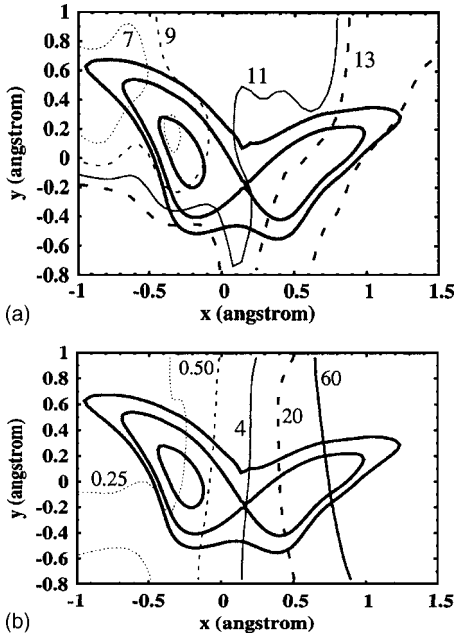

FIG. 6. Contour plots of the photoionization intensity defined in Eq. (21) (arbitrary units). Panel (a): ka' component. I=7 (dotted line), 9 (short-dashed line), 11 (thin solid line), and 13 (long-dashed line). Panel (b): ka'' component. I=0.25 (dotted line), 0.50 (short-dashed line), 4 (thin solid line), 20 (long-dashed line), and 60 (thick solid line). In both panels, contour plots of the ground state potential at 0.25, 0.936, and 1.50 eV are also shown (thick solid lines).

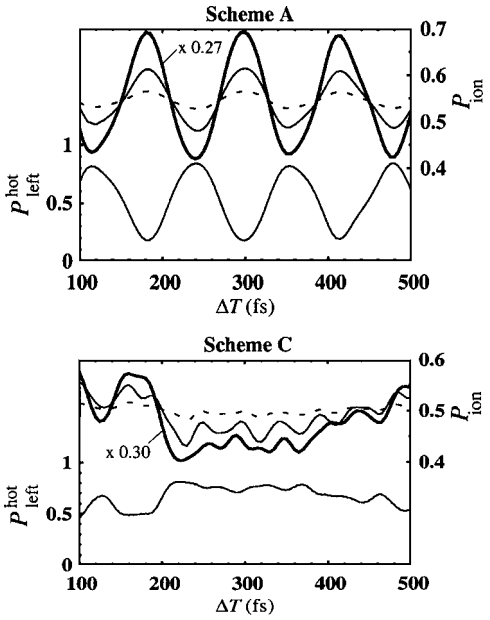

FIG. 7. Time evolution of integrated photoelectron signals in arbitrary units (scales to the right) obtained with schemes A (upper panel) and C (lower panel). Thick solid lines: calculation employing *ab initio* matrix elements with perpendicular orientation (ka'' component, see text), thin solid lines: calculation employing *ab initio* matrix elements with parallel orientation (ka' component), and dashed line: Condon-approximation calculation. For the sake of presentation the curves have been vertically shifted but only the results obtained with perpendicular orientation have been rescaled as indicated (factors of 0.27 and 0.30 for schemes A and C, respectively). In both panels, the vibrationally hot left-ratio population ($P_{\rm left}^{\rm hot}$) in the ground state is also shown (thin solid lines, scales to the left).

photoelectron spectra, since in general both continua would contribute to orientation-averaged photoionization signals.

In Fig. 7 we compare total photoelectron signals obtained with constant (Condon approximation) and geometry-dependent matrix elements for parallel (nonresonant ka' component) and perpendicular (resonant ka'' component) orientations,[66] and for schemes A (upper panel) and C (lower panel). The ion signals were obtained as functions of the time delay ($\Delta T=\Delta T_{\rm du}+\Delta T_{\rm pr}$) using a probe pulse of frequency $\hbar\omega_{\rm pr}$=8.75 eV and a full width at half maximum, FWHM$_{\rm pr}$=20 fs, and are out of phase with the vibrationally hot left-population ratios ($P_{\rm left}^{\rm hot}$) because ionization is more effective from the right basin. Ion signals obtained with the Condon approximation can track the periodic proton transfer of scheme A, though with worse resolution than with *ab initio* matrix elements, but they are not sensitive to details of the time evolution of the more delocalized population of scheme C. In particular, use of *ab initio* matrix elements permits probing of the sudden change from delocalization to localization in the left basin at around 200 fs, the details of the subsequent oscillations in the left basin, and the slow delocalization after 220 fs (positive slope). These results suggest that geometry-dependent matrix elements could be crucial in more elaborate studies of time-resolved photoelectron spectra describing real-time relaxation on multidimensional potential surfaces. As expected, the resolution of ionization signals is better for the ka'' component (rescaled by factors around 0.3), but signals arising from both symmetry components are qualitatively similar. In the following we restrict the discussion to the parallel orientation where the nonresonant ka' component of the cross section may be more representative of the photoelectron spectra that may arise in applications.

B. Photoelectron signals

Vibrationally hot wave packets generated with schemes A–D were probed with pulses of frequency $\hbar\omega_{\rm pr}$=8.75 eV, intensity $I_{\rm pr}=4.39\times10^{11}$ W/cm^2, and widths FWHM$_{\rm pr}$=10, 20, and 40 fs. Though the probe frequency was high enough to allow ionization of the excited wave packet everywhere on the S_0 potential surface, the background signal arising from the vibrational ground state population was very weak due to the high-energy gap, $\langle E_{\rm hot}\rangle - E_{\nu_0=0}\simeq 0.85$ eV. The classical energy of the system (molecular ion plus photoelectron) for ionization from the ν_0=0 level ($E_{\nu_0=0}$=0.30 eV) is $E_{\nu_0=0}+\hbar\omega_{\rm pr}$=9.05 eV, and since the energies of the two lowest vibrational eigenstates of the ion surface are 9.08 and 9.15 eV, ionization from the ν_0=0 level gives rise to a weak signal at very low kinetic energies. This process would be more effective with higher probe frequencies, but these would give rise to wave packets on the ion state surface (arising from the vibrationally hot population) with enough energy to surmount the barriers towards *cis-trans* isomerization from either oxygen atoms (see Fig. 2), and our configuration space is not sufficiently large to account for these reactions[67] (a procedure to eliminate intense background photoelectron signals arising from the ν_0=0 population was discussed elsewhere[32]). Photoelectrons arising from the excited state (dump pulse) were not taken into account because

Downloaded 06 Feb 2007 to 131.215.225.9. Redistribution subject to AIP license or copyright, see http://jcp.aip.org/jcp/copyright.jsp

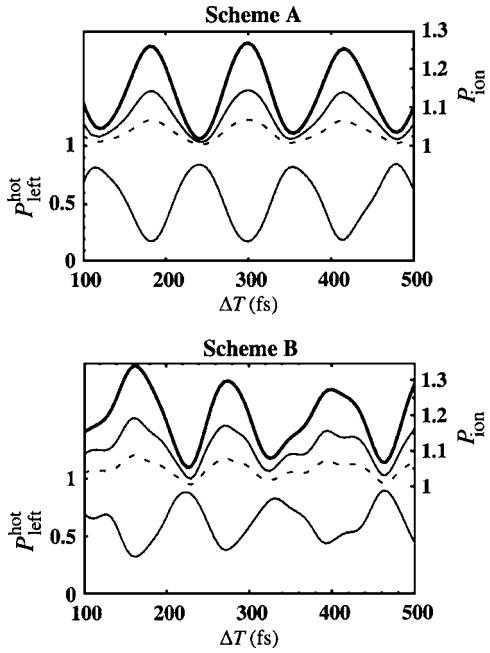

FIG. 8. Time evolution of integrated photoelectron signals in arbitrary units (scales to the right) obtained with schemes A (upper panel) and B (lower panel) for probe pulse widths of 10 fs (dashed lines), 20 fs (thin solid lines), and 40 fs (thick solid lines). For the sake of presentation the curves have been vertically shifted but not rescaled. In both panels, the lower thin solid line is the vibrationally hot left-ratio population ($P_{\rm left}^{\rm hot}$) in the ground state (scales to the left).

these can be energy resolved from those arising from the ground state (probe pulse), and Koopmans' theorem estimates indicate that ionization channels from lower molecular orbitals would be closed (the second ionization potential is about 2 eV higher for all relevant geometries).

The total ion signals are shown in Figs. 8 (schemes A and B) and 9 (schemes C and D), where the curves have been vertically shifted to the same scale for presentation, though not rescaled. The corresponding vibrationally hot left-ratio populations ($P_{\rm left}^{\rm hot}$) are also shown. The photoelectron signals generally provide useful insight into wave packet motion, with shorter probe pulses giving rise to weaker signals but reflecting small-amplitude oscillations with greater detail. In scheme D (Fig. 9), the longest pulse width (40 fs) convolutes several neighboring short peaks, giving rise to a high plateau in the photoelectron signal that does not faithfully reflect the wave packet dynamics. Though not shown here, proton transfer in schemes A and B (Fig. 8) could be tracked even with a pulse width of the same order of the proton transfer period (FWHM$_{\rm pr}$=60 fs). The magnitudes of the ion signals depend on the final vibrationally hot population, but for a given pump-dump scheme the highest and lowest ion signals always reflect the maximum localization on the right and left basins, respectively. Delocalized wave packets ($P_{\rm left}^{\rm hot}\sim 0.5$) may have nodes or peaks in the transition state region, but these situations could not be clearly distinguished by either total or energy-resolved photoelectron signals.

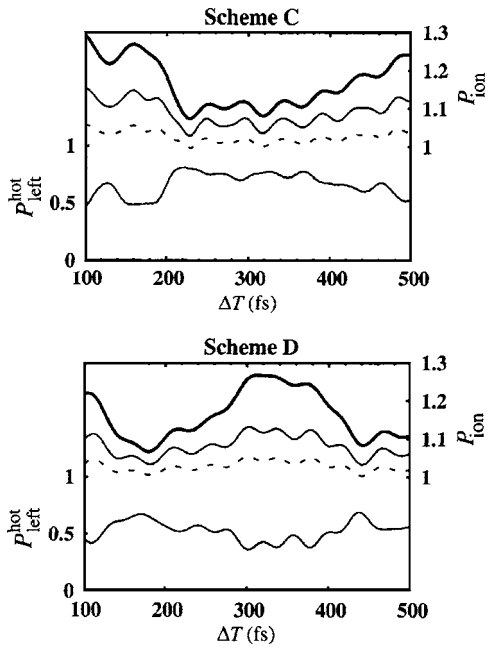

FIG. 9. Same as in Fig. 8 but for schemes C (upper panel) and D (lower panel).

Since the photoelectron energy distribution displays fairly similar trends for all schemes, we focus the discussion on scheme B. Energy-resolved signals obtained with FWHM$_{\rm pr}$=40 fs for ΔT=225 fs (localized to the left, $P_{\rm left}^{\rm hot}$=0.88), ΔT=255 fs (delocalized, $P_{\rm left}^{\rm hot}$=0.53), and ΔT=160 fs (localized to the right, $P_{\rm left}^{\rm hot}$=0.33) are shown in panel (a) of Fig. 10, and contour plots of the corresponding wave packets are shown in panel (c) (in these plots, the vibrational ground state component was projected out). Localization of the wave packet to the left of the transition state (ΔT=225 fs) gives rise to four peaks of similar magnitude below 0.4 eV, while photoelectron kinetic energies arising from the right basin (ΔT=160 fs) are strongly peaked around 0.30 eV, with a weak peak at higher energies (0.63 eV). Kinetic energy distributions arising from delocalized wave packets always have contributions from both basins and are intermediate between the two former cases.

Further insight into photoelectron energies may be gained by defining the classical kinetic energy ($\epsilon_{\rm clas}$),

$$\epsilon_{\rm clas} = E_{\rm hot}^{\rm vib} + \hbar\omega_{\rm pr} - E_{\rm ion}^{\rm vib}, \tag{22}$$

where $E_{\rm hot}^{\rm vib}$ and $E_{\rm ion}^{\rm vib}$ are the vibrational energies in the ground (excluding the ν_0=0 level) and ion states, respectively. The energy expectation value was $\langle E_{\rm hot}^{\rm vib}\rangle$=1.16 eV for scheme B, and the vibrational eigenvalues of the ion state surface, as well as the decomposition of the ground state wave packet into the eigenstates of the ion surface, may be obtained as

$$S_{\rm ion}(E,t) = \int d\tau \exp\left(i\frac{E\tau}{\hbar}\right)\langle\chi_g(t)| \times\exp\left[-\frac{i(\tau-t)}{\hbar}(T_{\mathbf{R}}+V_{\rm ion})\right]|\chi_g(t)\rangle, \tag{23}$$

where the time evolution is governed by the Hamiltonian of the ion state, $T_{\mathbf{R}}+V_{\rm ion}$. Estimates of the classical photoelectron energies may be obtained by shifting the corresponding intensity according to Eq. (22),

Downloaded 06 Feb 2007 to 131.215.225.9. Redistribution subject to AIP license or copyright, see http://jcp.aip.org/jcp/copyright.jsp

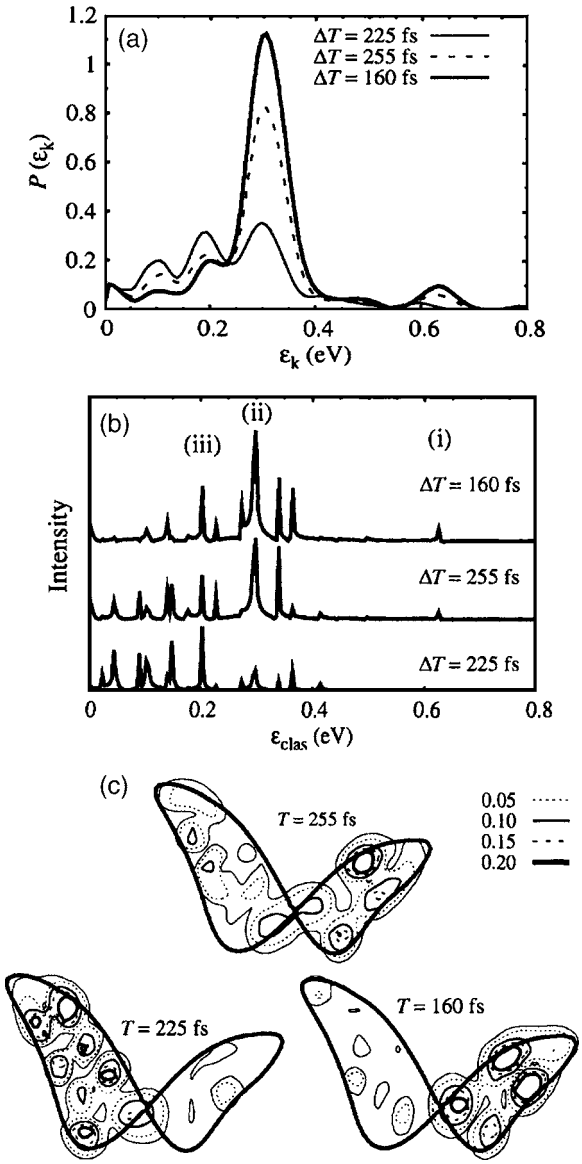

FIG. 10. Panel (a): photoelectron kinetic energy distributions for scheme B with $\mathrm{FWHM}_{pr}=40$ fs and $\Delta T=160$, 225, and 255 fs. Panel (b): decomposition of the ground state wave packets into vibrational eigenstates of the ion surface. The $\nu_0=0$ component was projected out in all cases, and the peaks were shifted to classical kinetic energies, according to Eq. (24). Panel (c): Contour plots of the vibrationally hot population in the ground state surface at $T=160$, 225, and 255 fs. The contour of the ground state potential surface at the transition state energy ($E_{TS}=0.936$ eV) is also shown (thickest solid lines).

$$I(\epsilon_{\mathrm{clas}},t) \equiv |S_{\mathrm{ion}}(\langle E_{\mathrm{hot}}^{\mathrm{vib}}\rangle + \hbar\omega_{\mathrm{pr}} - E,t)|^2, \tag{24}$$

where E is the same as in Eq. (23). There is a clear correspondence between the kinetic energy distributions [panel (a)] and the peaks of $I(\epsilon_{\mathrm{clas}},t)$ [panel (b)], though the geometry dependence of the photoionization matrix elements also plays a role. The peak around 0.63 eV ($\Delta T=160$, and 255 fs) arises from the ion eigenstate labeled (i) in Fig. 10, and the contour plots in the upper panel of Fig. 11 clearly indicate that (i) does not couple with the left basin of the ground state. The sharp peak around 0.30 eV, typical of population localized to the right of the barrier, seems to arise from a few neighboring eigenstates around the one labeled (ii) in Fig. 10, whose contour plots are shown in the central panel of

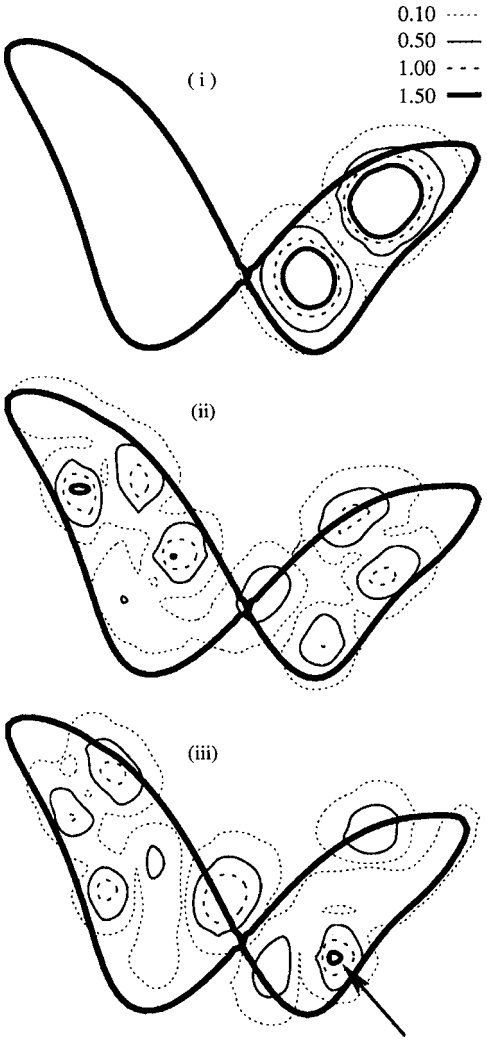

FIG. 11. Contour plots of selected vibrational eigenstates of the *ion state*. In all panels, the contour of the *ground state* potential surface at the transition state energy ($E_{TS}=0.936$ eV) is shown (thickest solid lines) to facilitate comparison with Figs. 5 and 10.

Fig. 11. The eigenstate probability is fairly delocalized and suggests that the more effective coupling to the right arises more from the shape of the wave packet (more favorable superposition of peaks and nodes yielding a larger overlap) than from localization of (ii) on the right basin. The $P(\epsilon_k)$ peak at 0.30 eV [panel (a) of Fig. 10] is relatively high even for $\Delta T=225$ fs, despite the modest coupling with eigenstate (ii) seen in panel (b), because it arises mainly from the transition state region, where the strength of the optical coupling is larger than in the left basin. Finally, it is interesting to note that the eigenstate labeled (iii) in Fig. 10 couples to the three wave packets ($T=160$, 225, and 255 fs) with similar strengths, though the corresponding peak in the kinetic energy distribution [panel (a)] is higher for the wave packet localized to the left ($T=225$ fs). The contour plots of the eigenstate (iii) (lower panel of Fig. 11) indicate that the overlap on the right basin ($T=160$ fs) arises mostly from a very localized peak (1.50 eV contour, indicated by the arrow in Fig. 11), while several peaks in the left basin and transition state contribute to the overlap with the wave packet on the left basin ($T=225$ fs). This accounts for the higher peak seen

Downloaded 06 Feb 2007 to 131.215.225.9. Redistribution subject to AIP license or copyright, see http://jcp.aip.org/jcp/copyright.jsp

in the photoelectron energy distributions around 0.20 eV.

In our study, two important phenomena were neglected. The first is the $2\,^1A'/1\,^1A''$ conical intersection that occurs near the barrier in planar geometries. We ignored this feature because the transition dipole from the ground state to the $2\,^1A'$ state, about 4 D, is 40 times larger than that to the $1\,^1A''$ state. Though the $1\,^1A''$ state will be populated through bifurcation of the wave packet at the $2\,^1A'/1\,^1A''$ conical intersection, our pump-dump scheme is only sensitive to the $2\,^1A'$ state because of the $1\,^1A''$ state's small transition dipole; the effect of the $1\,^1A''$ state is only to somewhat diminish, not to interfere with, the signal. The other phenomenon is *cis-trans* isomerization. Coe and Martínez[40] found that malonaldehyde (MA) undergoes rapid (<100 fs) torsional motion, which competes very effectively with proton transfer, when the S_2 excited state is populated. To determine whether excited Cl-MA also undergoes *cis-trans* isomerization, we computed minimum-energy-path potential curves obtained by rotating about the C=C bond while allowing other internal coordinates to relax completely. The results show that the relevant $2\,^1A'$ state potential is very flat; thus, *cis-trans* isomerization will indeed compete with proton transfer in Cl-MA. For this reason, as noted in Sec. I, planar Cl-MA should be considered a simplified model relevant to proton transfer in systems where the torsional motion is hindered. On the other hand, there are some significant differences worth mentioning between Cl-MA and MA. First, in contrast to MA, the $1\,^1A'$, $1\,^1A''$, and $2\,^1A'$ states of Cl-MA do not form a three-state conical intersection; also, the $2\,^1A'$ and $1\,^1A''$ states have a conical intersection at dihedral angles of about 65° and 125°; and finally, there is no $1\,^1A'/1\,^1A''$ conical intersection. These differences will cause the population to remain in the $2\,^1A'$ and $1\,^1A''$ states after a wave packet is deposited on the $2\,^1A'$ surface. Thus, proton transfer may resurge when the *cis-trans* dihedral angle returns to 0° (or 360°).

V. CONCLUDING REMARKS

We have employed classically averaged potential surfaces of reduced dimensionality and *ab initio* photoionization matrix elements to study time-resolved photoelectron spectra of proton transfer. The generation of these effective potentials was discussed elsewhere[33] and here they were explored to simulate the real-time monitoring of intramolecular proton transfer in the ground state of Cl-MA. In these simulations, the initial condition was assumed to be the $\nu_0=0$ vibrational level of the ground state surface, and efficient population transfer to vibrationally hot wave packets was achieved by pumping to an excited state and dumping with a time-delayed pulse (for several different combinations of pulse parameters). Total photoelectron signals employing geometry-dependent *ab initio* matrix elements proved superior for tracking proton transfer to those obtained with the Condon approximation, especially when wave packet motion did not show simple periodic patterns. This suggests the importance of using such photoelectron matrix element in more realistic simulations of real-time energy redistribution between the proton and the molecular backbone. In general, the time-resolved photoelectron spectra could clearly track proton transfer in the ground state of Cl-MA, and photoelectron kinetic energy distributions were seen to arise from the strength of the coupling matrix elements (larger on the right basin) and Franck-Condon overlaps between the wave packet and the vibrational eigenstates of the ion surface. Neglect of conical intersections and, especially, *cis-trans* isomerization are certainly limitations for the present chelate ring system; nonetheless, the results presented here indicate that our approach is suitable to study the proton transfer in systems where the torsional motion is hindered.

ACKNOWLEDGMENTS

This work has been supported by the National Science Foundation (U.S.) and by a Grant-in-Aid for Basic Science and the 21st Century COE Program for Frontier in Fundamental Chemistry from the Ministry of Education, Culture, Sports, Science, and Technology of Japan. M.T.N.V. thanks JSPS for a Postdoctoral Fellowship.

[1] *Proton Transfer in Hydrogen-Bonded Systems*, edited by T. Bountis (Plenum, New York, 1992).
[2] H. H. Limbach and J. Manz, Ber. Bunsenges. Phys. Chem. **102**, 289 (1998).
[3] G. Zundel, Adv. Chem. Phys. **111**, 1 (2000).
[4] R. P. Steer, J. Photochem. Photobiol., A **154**, 1 (2002).
[5] J. Bicerano, H. F. Schaefer III, and W. H. Miller, J. Am. Chem. Soc. **105**, 2550 (1983).
[6] T. Carrington, Jr. and W. H. Miller, J. Chem. Phys. **84**, 4364 (1986).
[7] N. Shida, P. F. Barbara, and J. E. Almlöf, J. Chem. Phys. **91**, 4061 (1989).
[8] E. Bosch, M. Moreno, J. M. Lluch, and J. Bertrán, J. Chem. Phys. **93**, 5685 (1990).
[9] T. D. Sewell, Y. Guo, and D. L. Thompson, J. Chem. Phys. **103**, 8557 (1995).
[10] M. Ben-Nun and T. J. Martínez, J. Phys. Chem. A **103**, 6055 (1999).
[11] K. Yagi, T. Taketsugu, and K. Hirao, J. Chem. Phys. **115**, 10647 (2001); G. V. Mil'nikov, K. Yagi, T. Taketsugu, H. Nakamura, and K. Hirao, *ibid.* **119**, 10 (2003).
[12] V. A. Benderskii, E. V. Vetoshkin, I. S. Irgibaeva, and H. P. Tommsdorff, Chem. Phys. **262**, 393 (2000); Russ. Chem. Bull. **50**, 1148 (2002).
[13] D. Babić, S. D. Bosanac, and N. Došlić, Chem. Phys. Lett. **358**, 337 (2002).
[14] C. S. Tautermann, A. F. Voegele, T. Loerting, and K. R. Liedl, J. Chem. Phys. **117**, 1962 (2002); **117**, 1967 (2002).
[15] S. F. Tayyari, M. Z. Tabrizi, F. Tayyari, and F. Milani-Nejad, J. Mol. Struct.: THEOCHEM **637**, 171 (2003).
[16] M. Coutinho-Neto, A. Viel, and U. Manthe, J. Chem. Phys. **121**, 9207 (2004).
[17] K. Nishi, H. Sekiya, H. Kawakami, A. Mori, and Y. Nishimura, J. Chem. Phys. **109**, 1589 (1998); **111**, 3961 (1999).
[18] H. Ushiyama and K. Takatsuka, Angew. Chem., Int. Ed. **44**, 1237 (2005).
[19] H. Ushiyama and K. Takatsuka, J. Chem. Phys. **115**, 5903 (2001).
[20] A. H. Zewail, J. Phys. Chem. A **104**, 5660 (2000).
[21] K. Fuke, H. Yoshiuchi, and K. Kaya, J. Phys. Chem. **88**, 5840 (1984); K. Fuke and K. Kaya, *ibid.* **93**, 614 (1989); A. Douhal, S. K. Kim, and A. H. Zewail, Nature (London) **378**, 260 (1995); T. Fiebig, M. Chachisvilis, M. M. Manger, and A. H. Zewail, J. Phys. Chem. A **103**, 7419 (1999); S. Takeuchi and T. Tahara, J. Phys. Chem. **102**, 7740 (1998); Chem. Phys. Lett. **277**, 340 (1997); **347**, 108 (2001).
[22] H. Ishikawa, K. Iwata, and H. Hamaguchi, J. Phys. Chem. A **106**, 2305 (2002).
[23] Y. Komoto, K. Sakota, and H. Sekiya, Chem. Phys. Lett. **406**, 15 (2005).
[24] K. Sakota and H. Sekiya, J. Phys. Chem. A **109**, 2718 (2005); **109**, 2722 (2005).
[25] S. Lochbrunner, T. Schultz, M. Schmitt, J. P. Shaffer, M. Z. Zgierski, and A. Stolow, J. Chem. Phys. **114**, 2519 (2001).
[26] D. M. Neumark, Annu. Rev. Phys. Chem. **52**, 255 (2001).
[27] See several review articles in *Photoionization and Photodetachment*, Ad-

Downloaded 06 Feb 2007 to 131.215.225.9. Redistribution subject to AIP license or copyright, see http://jcp.aip.org/jcp/copyright.jsp

vanced Series in Physical Chemistry Vol. 10, edited by C. Y. Ng (World Scientific, Singapore, 1999).
[28] T. Baumert, R. Thalweiser, V. Weiss, and G. Gerber, in *Femtosecond Chemistry*, edited by J. Manz and L. Wöste (VCH, Weinheim, 1995), Chap. 12.
[29] V. Blanchet, M. Z. Zgierski, T. Seideman, and A. Stolow, Nature (London) **401**, 52 (1999).
[30] M. Seel and W. Domcke, J. Chem. Phys. **95**, 7806 (1991).
[31] Ch. Meier and V. Engel, J. Chem. Phys. **101**, 2673 (1994).
[32] Y. Arasaki, K. Yamazaki, M. T. do N. Varella, and K. Takatsuka, Chem. Phys. **311**, 255 (2005).
[33] M. T. do N. Varella, Y. Arasaki, H. Ushiyama, V. McKoy, and K. Takatsuka, J. Chem. Phys. **124**, 154302 (2006).
[34] Y. Arasaki, K. Takatsuka, K. Wang, and V. McKoy, Chem. Phys. Lett. **302**, 363 (1999); J. Chem. Phys. **112**, 8871 (2000).
[35] B. A. Ruf and W. H. Miller, J. Chem. Soc., Faraday Trans. 2 **84**, 1523 (1988).
[36] G. K. Paramonov, H. Naundorf, and O. Kühn, Eur. Phys. J. D **14**, 205 (2001).
[37] H. Naundorf, G. A. Worth, H.-D. Meyer, and O. Kühn, J. Phys. Chem. A **106**, 719 (2002).
[38] Y. Suzuki, M. Stener, and T. Seideman, J. Chem. Phys. **118**, 4432 (2003).
[39] T. Imasaka, D. S. Moore, and T. Vo-Dinh, Pure Appl. Chem. **75**, 975 (2003).
[40] J. D. Coe and T. J. Martínez, J. Am. Chem. Soc. **127**, 4560 (2005); J. Phys. Chem. A **110**, 618 (2006).
[41] Y. Arasaki, K. Takatsuka, K. Wang, and V. McKoy, J. Chem. Phys. **114**, 7941 (2001).
[42] Y. Arasaki, K. Takatsuka, K. Wang, and V. McKoy, Phys. Rev. Lett. **90**, 248303 (2003); J. Chem. Phys. **119**, 7913 (2003).
[43] M. E. Rose, *Elementary Theory of Angular Momentum* (Dover, New York, 1995).
[44] R. R. Lucchese, D. K. Watson, and V. McKoy, Phys. Rev. A **22**, 421 (1980); R. R. Lucchese, G. Raseev, and V. McKoy, *ibid.* **25**, 2572 (1982); S. N. Dixit and V. McKoy, J. Chem. Phys. **82**, 3546 (1985); R. R. Lucchese, K. Takatsuka, and V. McKoy, Phys. Rep. **131**, 147 (1986); K. Wang and V. McKoy, J. Chem. Phys. **95**, 4977 (1991); Annu. Rev. Phys. Chem. **46**, 275 (1995).
[45] D. Kosloff and R. Kosloff, J. Comput. Phys. **52**, 35 (1983); R. Kosloff, J. Phys. Chem. **92**, 2087 (1988).
[46] K. Takahashi and K. Ikeda, J. Chem. Phys. **99**, 8680 (1993).
[47] D. Lauvergnat and A. Nauts, J. Chem. Phys. **116**, 8560 (2002).
[48] J. L. Herek, S. Pedersen, L. Banares, and A. H. Zewail, J. Chem. Phys. **97**, 9046 (1992).
[49] M. W. Schmidt, K. K. Baldridge, J. A. Boatz *et al.*, J. Comput. Chem. **14**, 1347 (1993).
[50] H. Ushiyama, Y. Arasaki, and K. Takatsuka, Chem. Phys. Lett. **346**, 169 (2001).
[51] P. Brumer and M. Shapiro, Chem. Phys. Lett. **126**, 541 (1986); Annu. Rev. Phys. Chem. **43**, 257 (1992).
[52] D. J. Tannor and R. A. Rice, J. Chem. Phys. **83**, 501 (1985); D. J. Tannor, R. Kosloff, and R. A. Rice, *ibid.* **85**, 5805 (1986).
[53] J. R. Kuklinski, U. Gaubatz, F. T. Hioe, and K. Bergamnn, Phys. Rev. A **40**, 6741 (1989); V. S. Malinovsky and D. J. Tannor, *ibid.* **56**, 4929 (1997).
[54] A. P. Pierce, M. A. Dahleh, and H. Rabitz, Phys. Rev. A **37**, 4950 (1988); H. Rabitz and S. Shi, Adv. Mol. Vib. Collision Dyn. **1A**, 187 (1991).
[55] G. K. Paramonov and V. A. Savva, Phys. Lett. **97A**, 340 (1983); W. Jakubetz, B. Just, J. Manz, and H. J. Schreier, J. Phys. Chem. **94**, 2294 (1990).
[56] Y. J. Yan, Annu. Rep. Prog. Chem., Sect. C: Phys. Chem. **94**, 397 (1998); J. X. Cheng, Z. W. Shen, and Y. J. Yan, J. Chem. Phys. **109**, 1654 (1998).
[57] B. Kohler, V. V. Yakovlev, J. Che, J. L. Krause, M. Messima, K. R. Wilson, N. Schwentner, R. M. Whitnell, and Y. J. Yan, Phys. Rev. Lett. **74**, 3360 (1995); C. J. Berdeen, J. Che, K. R. Wilson, V. V. Yakovlev, V. A. Apkarian, C. C. Martens, R. Zadoyan, B. Kohler, and M. Messina, J. Chem. Phys. **106**, 8486 (1997); T. Hornung, R. Meier, and M. Motzkus, Chem. Phys. Lett. **326**, 445 (2000).
[58] A. Assion, T. Baumert, M. Bergt, T. Brixner, B. Kiefer, V. Seyfried, M. Strehle, and G. Gerber, Science **282**, 919 (1998); T. Brixner, N. H. Damrauer, P. Niklaus, and G. Gerber, Nature (London) **414**, 57 (2001); T. Brixner, G. Krampert, T. Pfeifer, R. Selle, G. Gerber, M. Wollenhaupt, O. Graefe, C. Horn, D. Liese, and T. Baumert, Phys. Rev. Lett. **92**, 208301 (2004).
[59] P. O. Stoutland, R. B. Dyer, and W. H. Woodruff, Science **257**, 1913 (1992); M. V. Korolkov, J. Manz, and G. K. Paramonov, Chem. Phys. **217**, 341 (1997).
[60] Z. W. Shen, J. Chen, M. Heid, W. Kiefer, and V. Engel, Eur. Phys. J. D **14**, 167 (2001).
[61] H. Schwoerer, R. Pausch, M. Heid, and W. Kiefer, Chem. Phys. Lett. **285**, 240 (1998); R. Pausch, M. Heid, T. Chen, W. Kiefer, and H. Schwoerer, J. Chem. Phys. **110**, 9560 (1999).
[62] Z. Shen, Y. Yan, J. Cheng, F. Shuang, Y. Zhao, and G. He, J. Chem. Phys. **110**, 7192 (1999).
[63] V. Bonacic-Koutecky, M. Hartmann, J. Pittner, and H. van Dam, Int. J. Quantum Chem. **84**, 714 (2001); R. Mitri, M. Hartmann, J. Pittner, and V. Bonai-Kouteck, J. Phys. Chem. A **106**, 10477 (2002).
[64] D. Zeidler, S. Frey, W. Wohlleben, M. Motzkus, F. Busch, T. Chen, and W. Kiefer, J. Chem. Phys. **116**, 5231 (2002).
[65] K. Takatsuka and N. Hashimoto, J. Chem. Phys. **103**, 6057 (1995). For a related method see D. Neuhauser, *ibid.* **93**, 2611 (1990); **95**, 4927 (1991).
[66] The orientation of the molecule (asymmetric top) in any given frame is not completely determined by the direction of the principal axis, which was assumed parallel to the polarization vectors of the pump and dump pulses to lower the computational effort. Though we did not perform a systematic study, exploratory results obtained for a couple of different angular positions around the principal axis suggested that these rotations would not impact, qualitatively, the photoelectron spectra discussed here. The angular resolution of these spectra will require a realistic treatment of molecular alignment and orientation averages.
[67] Here *cis-trans* isomerization refers to the position of the proton with respect to the chelate ring [rotation around the C_1-O_1 and C_3-O_2 bonds that may take place in structures (a) and (c) of Fig. 2, respectively] and not to the torsional motion around C=C bonds. If higher probe frequencies were employed to enhance the ion signals arising from the vibrational ground state ($\nu_0=0$), comcomitant ionization from vibrationally hot eigenstates would give rise to high-energy wave packets in the ion surface, and *cis-trans* isomerization would thus take place. Since we are not interested in this process, whose description would require considerable expansion of the reaction configuration space along the *Ox* direction, the probe frequency was kept low enough.

Downloaded 06 Feb 2007 to 131.215.225.9. Redistribution subject to AIP license or copyright, see http://jcp.aip.org/jcp/copyright.jsp